

Diffuse Ionized Gas in the Anti-center of the Milky Way

SHIMING WEN,¹ WEI ZHANG,¹ LIN MA,^{2,1,3} YUNNING ZHAO,^{1,3} LAM, MAN I.,⁴ CHAOJIAN WU,¹ JUANJUAN REN,⁴
JIANJUN CHEN,⁴ YUZHONG WU,¹ GUOZHEN HU,⁵ YONGHUI HOU,^{6,3} YONGHENG ZHAO,^{1,3} AND HONG WU^{1,3}

¹CAS Key Laboratory of Optical Astronomy, National Astronomical Observatories, Chinese Academy of Sciences, Beijing 100101, People's Republic of China; xtwfn@bao.ac.cn

²The Key Laboratory of Cosmic Rays (Tibet University), Ministry of Education, Lhasa 850000, Tibet, China

³School of Astronomy and Space Science, University of Chinese Academy of Sciences, Beijing 100049, China

⁴CAS Key Laboratory of Space Astronomy and Technology, National Astronomical Observatories, Chinese Academy of Sciences, Beijing 100101, People's Republic of China

⁵College of Physics, Hebei Normal University, 20 South Erhuan Road, Shijiazhuang 050024, People's Republic of China

⁶Nanjing Institute of Astronomical Optics, & Technology, National Astronomical Observatories, Chinese Academy of Sciences, Nanjing 210042, People's Republic of China

ABSTRACT

Using data from the LAMOST Medium-Resolution Spectroscopic Survey of Nebulae, we create a sample of 17,821 diffuse ionized gas (DIG) spectra in the anti-center region of the Milky Way, by excluding fibers in the directions of H II regions and supernova remnants. We then analyze the radial and vertical distributions of three line ratios ([N II]/H α , [S II]/H α , and [S II]/[N II]), as well as the oxygen abundance.

[N II]/H α and [S II]/H α do not exhibit a consistent, monotonic decrease with increasing Galactocentric distance (R_{gal}). Instead, they show enhancement within the interarm region, positioned between the Local Arm and the Perseus Arm. [S II]/[N II] has a radial gradient of $0.1415 \pm 0.0646 \text{ kpc}^{-1}$ for the inner disk ($8.34 < R_{gal} < 9.65 \text{ kpc}$), and remains nearly flat for the outer disk ($R_{gal} > 9.65 \text{ kpc}$). In the vertical direction, [N II]/H α , [S II]/H α , and [S II]/[N II] increase with increasing Galactic disk height ($|z|$) in both southern and northern disks.

Based on the N2S2H α method, which combines [S II]/[N II] and [N II]/H α , we estimate the oxygen abundance. The oxygen abundance exhibits a consistent radial gradient with R_{gal} , featuring a slope of $-0.0559 \pm 0.0209 \text{ dex kpc}^{-1}$ for the inner disk and a similar slope of $-0.0429 \pm 0.0599 \text{ dex kpc}^{-1}$ for the outer disk. A single linear fitting to the entire disk yields a slope of $-0.0317 \pm 0.0124 \text{ dex kpc}^{-1}$. In the vertical direction, the oxygen abundance decreases with increasing $|z|$ in both southern and northern disks.

Keywords: Warm Ionized Medium(1788)–Metallicity(1031)–Interstellar line emission(844)

1. INTRODUCTION

The interstellar medium (ISM) of the Milky Way consists of both interstellar gas and dust. Interstellar gas plays an important role in the form and death of stars as well as the evolutionary cycle of the interstellar medium. The properties of interstellar gas are affected by the radiation and matter ejected from stars, which in turn influence the characteristics of new generation stars. Interstellar gas can be further categorized into cold neutral gas comprising atomic and molecular gas, and ion-

ized gas (Sparke & Gallagher 2007). Ionized gas encompasses several components: the extremely hot ionized galactic halo, HII regions, supernova remnants (SNRs), planetary nebulae (PNe), and diffused ionized gas (DIG) (Draine 2011). DIG was first discovered from the free-free absorption when surveying the Galactic synchrotron background at radio wavelengths (Hoyle & Ellis 1963). Later, faint emission lines originated from DIG were observed at optical wavelengths confirming its existence (Reynolds et al. 1973). It has been estimated that DIG constitutes approximately 20% of the overall gaseous content while representing up to 90% among all ionized gases in Milky Way, thus established as a primary

source for such ions within our galaxy (Reynolds 1991; Haffner et al. 2009).

Some surveys have been designed to explore the Galactic DIG. For example, the Wisconsin H-Alpha Mapper (WHAM) Sky Survey in optical band (Haffner et al. 2003), and the Green Bank Telescope Diffuse Ionized Gas Survey (GDIGS) in radio band (Anderson et al. 2021). Additionally, data on piggyback recombination lines (RRLs) from the ongoing Galactic Plane Pulsar Snapshot (GPPS) survey offer valuable insights for analyzing Galactic DIG (Hou et al. 2022). Various emission lines have been used to investigate the distribution and characteristics of DIG in different bands. In the optical bands, [N II], [S II], [O II], [O III], O I, He I and H α lines are employed (Reynolds et al. 1998; Haffner et al. 1999; Hausen et al. 2002; Madsen et al. 2006). While in radio bands, RRLs of hydrogen, helium, and carbon serve as crucial probes (Luisi et al. 2017, 2019; Anderson et al. 2021). The intensity of diffuse Spitzer GLIMPSE 8.0 μ m emission is found to be correlated with the intensity of the RRL emission from the DIG (Luisi et al. 2017). The mid-infrared fine structure lines of [Ne II], [S III], and possibly [S IV] have been detected by the James Webb Space Telescope (JWST) (Kulkarni et al. 2024). DIG can also be detected in the fine structure far-infrared lines (eg., [C II] and [N II]) in absorption (Persson et al. 2014; Gerin et al. 2015), or in emission (Velusamy et al. 2012, 2015; Langer et al. 2017).

WHAM data has provided valuable insights into the physical properties and spatial distribution of Galactic DIG. Notably, the detection of the [O I] λ 6300 emission line within DIG regions near the Galactic plane indicates a predominance of ionized hydrogen, as inferred from the low [O I]/H α ratio (Reynolds et al. 1998; Hausen et al. 2002). Furthermore, investigations have revealed that the [S II]/H α and [N II]/H α ratios exhibit a tendency to increase with decreasing H α intensity, a trend that is accentuated with increasing vertical distance from the Galactic plane ($|z|$) (Reynolds et al. 1999). Comparisons with classical HII regions have highlighted distinct differences in the ionization characteristics of DIG. Specifically, DIG displays higher [N II]/H α and [S II]/H α ratios, coupled with lower [O III]/H α and He I/H α ratios. These findings suggest that DIG regions tend to have higher temperatures, exist in a lower ionization state, and are likely ionized by a softer spectrum of radiation compared to classical H II regions (Madsen et al. 2006).

WHAM has conducted a comprehensive all-sky survey of H α emission from the Milky Way, however, other crucial emission lines necessary for inferring the properties of DIG are only observed in selected regions of

the sky. Consequently, the continued distribution of DIG along the Galactic disk remains an open question. It is widely acknowledged that the metallicity of HII regions exhibits a negative radial gradient on the Galactic plane (e.g. Balser et al. 2011; Esteban et al. 2017; Méndez-Delgado et al. 2022). As there are various possible ionize sources for DIG, such as leaking photons from HII regions (Haffner et al. 2009), hot low-mass evolved stars (HOLMES) (Flores-Fajardo et al. 2011; Yan & Blanton 2012) and shocks (Collins & Rand 2001), hereafter, the distribution of DIG does not necessarily associated with HII regions (Luisi et al. 2017). Recent observations of M83 by MUSE have found that the fraction of H α luminosity originating from the DIG varies with galactic radius, and peaks in the interarm regions (Della Bruna et al. 2022). Consequently, in this study, we aim to investigate the distribution patterns of various parameters, such as [N II]/H α , [S II]/H α and [S II]/[N II] ratios, as well as oxygen abundance, along the Galactic disk within the DIG.

The contamination of DIG can significantly impact the characteristics of HII regions. This contamination can lead to misclassification of positions in the Baldwin–Phillips–Terlevich (BPT) diagram (Zhang et al. 2017), as well as overestimation of metallicity measurements (Sanders et al. 2017). Conversely, this contamination also affects the analysis of DIG properties. According to the Galactic HII region catalog (Anderson et al. 2014), the majority of HII regions have angular sizes smaller than several arcminutes. Therefore, achieving spatial resolutions at least at the arcminute level is necessary to effectively distinguish HII regions from DIG. The Large Area Multi-Object fiber Spectroscopic Telescope (LAMOST) has started the medium-resolution survey (LAMOST-MRS) in October 2018 (Liu et al. 2020; Wang et al. 1996; Su & Cui 2004; Cui et al. 2012; Zhao et al. 2012; Luo et al. 2015). The ongoing project of LAMOST-MRS of Nebulae (LAMOST MRS-N) provides an excellent opportunity to study Galactic DIG, considering its high spatial resolution ($\sim 3'$)¹, and wide sky coverage ($\sim 1700 \text{ deg}^2$) (Wu et al. 2021; Ren et al. 2021; Zhang et al. 2021; Wu et al. 2022). Based on this survey, we can construct a large sample of Galactic DIG to investigate the distribution of DIG on the disk, including radial and vertical gradients of DIG parameters along the Galactic disk.

¹ In this paper, spatial resolution is defined by the median fiber-to-fiber distance. Each fiber has a size of $3'' \times 3''$, with significant spacing between them, resulting in a median distance of $3'$ between adjacent.

The paper is structured as follows. The criteria for selecting Galactic DIG are described in Section 2. The methods for deriving kinematic distance and oxygen abundance are introduced in Section 3. In Section 4, we investigate the distributions of line ratios, and oxygen abundance along and perpendicular to the Galactic disk. We discuss the results in Section 5 and present the conclusion in Section 6.

2. SAMPLE CONSTRUCTION

The primary goal of LAMOST MRS-N is to survey ionized gas and bright stars in the Galactic disk ($|b| \leq 5^\circ$), within the Galactic longitude range of $80^\circ < l < 220^\circ$. The optical spectrum spans from 4950 to 5350 Å in the blue channel and 6300 to 6800 Å in the red channel, featuring a resolution power of $R = \lambda/\Delta\lambda \sim 7500$, as outlined by (Wu et al. 2021). For detailed information regarding the recalibration of wavelengths using skylines, readers are referred to the study by Ren et al. (2021). Additionally, the method of subtracting geocoronal H_α emission ($H_{\alpha,sky}$) by exploiting the correlation between the ratio of $H_{\alpha,sky}$ and $OH\lambda 6554$ line intensities and solar altitude is described in the work of Zhang et al. (2021). The throughput pipeline for data reduction and the resulting data products are summarized in the work by Wu et al. (2022).

We specifically focuses on four emission lines in the red channel, namely $[N II]\lambda 6584$, H_α , $[S II]\lambda\lambda 6717, 6731$. Due to the absence of flux calibration for LAMOST MRS-N, three key ratios will be utilized in subsequent analyses: $\text{Flux}([N II]\lambda 6584)/\text{Flux}(H_\alpha)$ (hereafter $[N II]/H_\alpha$), $\text{Flux}([S II]\lambda\lambda 6717, 6731)/\text{Flux}(H_\alpha)$ (hereafter $[S II]/H_\alpha$), and $\text{Flux}([S II]\lambda\lambda 6717, 6731)/\text{Flux}([N II]\lambda 6584)$ (hereafter $[S II]/[N II]$).

The sky coverage of fields obtained by LAMOST MRS-N to the end of 2021 have been shown in Figure 1, with color representation based on the $[N II]/H_\alpha$ line ratio. During observations, some regions are overlapped, resulting in these areas being observed multiple times. As these overlapping regions are over-sampled compared to areas observed only once, it is necessary to resample the data to a uniform density. Given a median spatial resolution of $3'$, and considering that most fibers have distances less than $5'$, we resample the data into $5' \times 5'$ bins. For each 2D bin, if only one fiber is found, we retain this fiber in the new dataset and assign the center of the bin as its new coordinate. In cases where more than one fiber are found within a bin, we retain the fiber with the highest Signal-to-Noise (S/N) ratio of H_α emission and assign the center of the bin as its new coordinate.

Various methods have been employed to distinguish between HII regions and DIG. These approaches are primarily rely on the H_α surface brightness (Kaplan et al. 2016; Zhang et al. 2017), the H_α line equivalent width (Belfiore et al. 2016; Kumari et al. 2019), or the $[N II]/H_\alpha$ and $[S II]/H_\alpha$ line ratios (Kumari et al. (2019), employing the classical BPT diagrams (Baldwin et al. 1981; Kauffmann et al. 2003; Kewley et al. 2006). If the spatial resolution is sufficiently high, an effective strategy for isolating DIG involves the identification of individual H II regions and subsequent subtraction (Belfiore et al. 2022).

In this work, we cross-match the LAMOST MRS-N database with the current largest Galactic HII catalogue selected from WISE MIR emission (Anderson et al. 2014; Wright et al. 2010), and eliminate fibers located within three times the radius of the HII regions (r_{WISE}) to minimize contamination from corresponding HII regions. We also exclude the fibers located within the SNR regions defined by $\frac{(x-x_0)^2}{a^2} + \frac{(y-y_0)^2}{b^2} \leq 1$, where a and b are the semi-major and semi-minor axes of the ellipse and (x_0, y_0) is the central position of the SNR, according to the Galactic SNRs catalog by Green (2019).

Additional criteria have also been considered as follows:

- (1) All four emission lines are required to have a signal-to-noise ratio (S/N) greater than 3.

- (2) $|V_{[N II]} - V_{H_\alpha}| < 20 \text{ km s}^{-1}$
 $|V_{[S II]} - V_{H_\alpha}| < 20 \text{ km s}^{-1}$
 $|V_{[N II]} - V_{[S II]}| < 20 \text{ km s}^{-1}$

This criterion is intended to eliminate fibers that may have a large systematic error in measuring radial velocity.

- (3) $0.24 < [S II]/H_\alpha$

The fibers located in the direction of HII regions exhibit a peak at ~ 0.20 for $[S II]/H_\alpha$ ratio, and the distributions of DIG and HII regions intersect at ~ 0.24 (Zhao et al., in preparation, see also Figure 5). Therefore, the range $0.24 < [S II]/H_\alpha$ is employed to further exclude potential HII regions from the analysis.

- (4) $80^\circ < l < 160^\circ$ and $200^\circ < l < 220^\circ$

The sources in the range of $160 \leq l \leq 200$ have been removed due to the uncertainties in kinematic distance measurement being too large in this direction.

Finally, we construct a large sample of Galactic DIG, comprising 17,821 fibers, hereafter referred to as Sample-I. The spatial distribution of this sample are illustrated in Figure 2, colored by the $[N II]/H_\alpha$ and the $[S II]/H_\alpha$

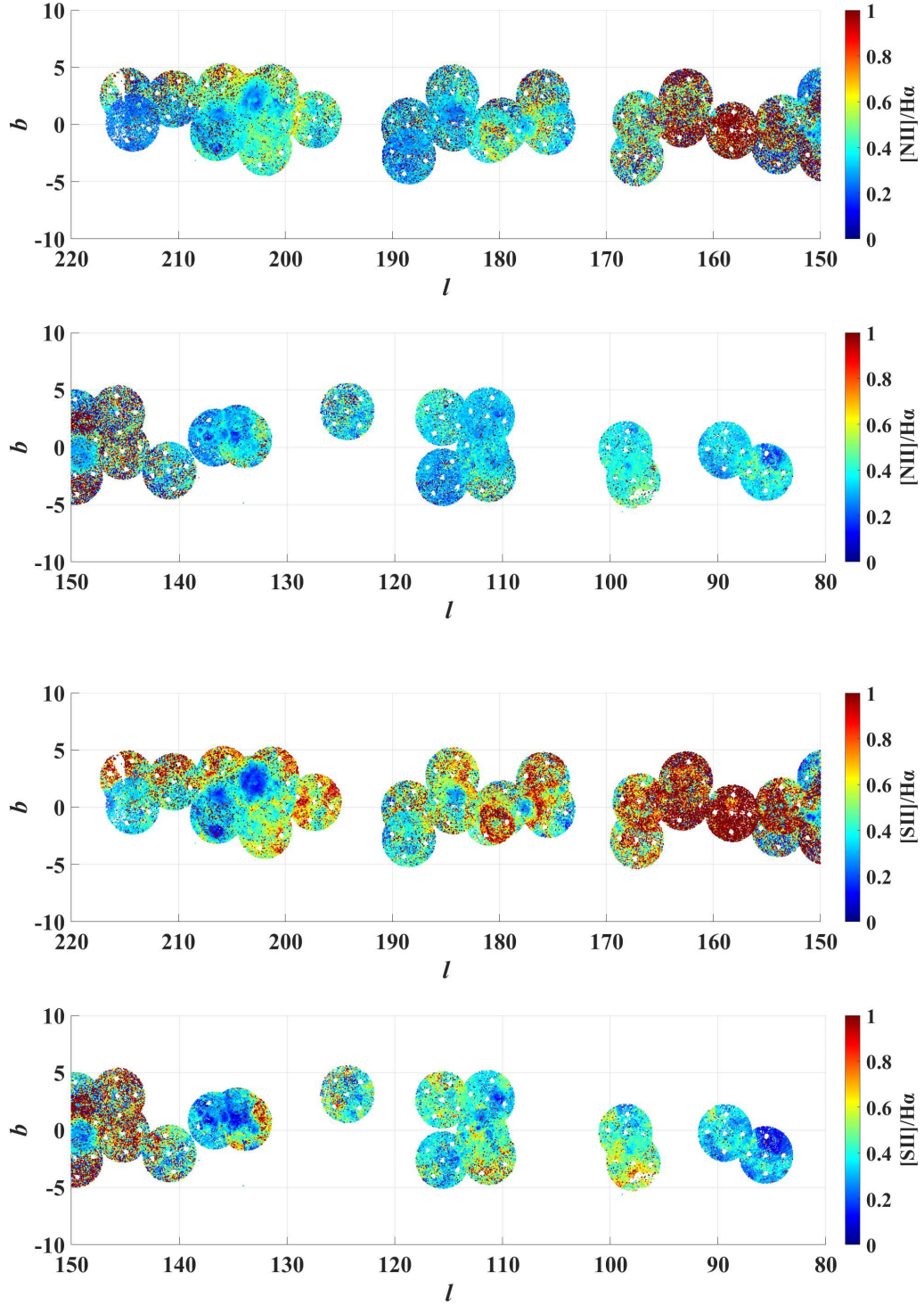


Figure 1. Footprints of LAMOST MRS-N up to the end of 2021, colored by $[\text{N II}]/\text{H}\alpha$ ratios in the top two panels and $[\text{S II}]/\text{H}\alpha$ ratios in the bottom two panels.

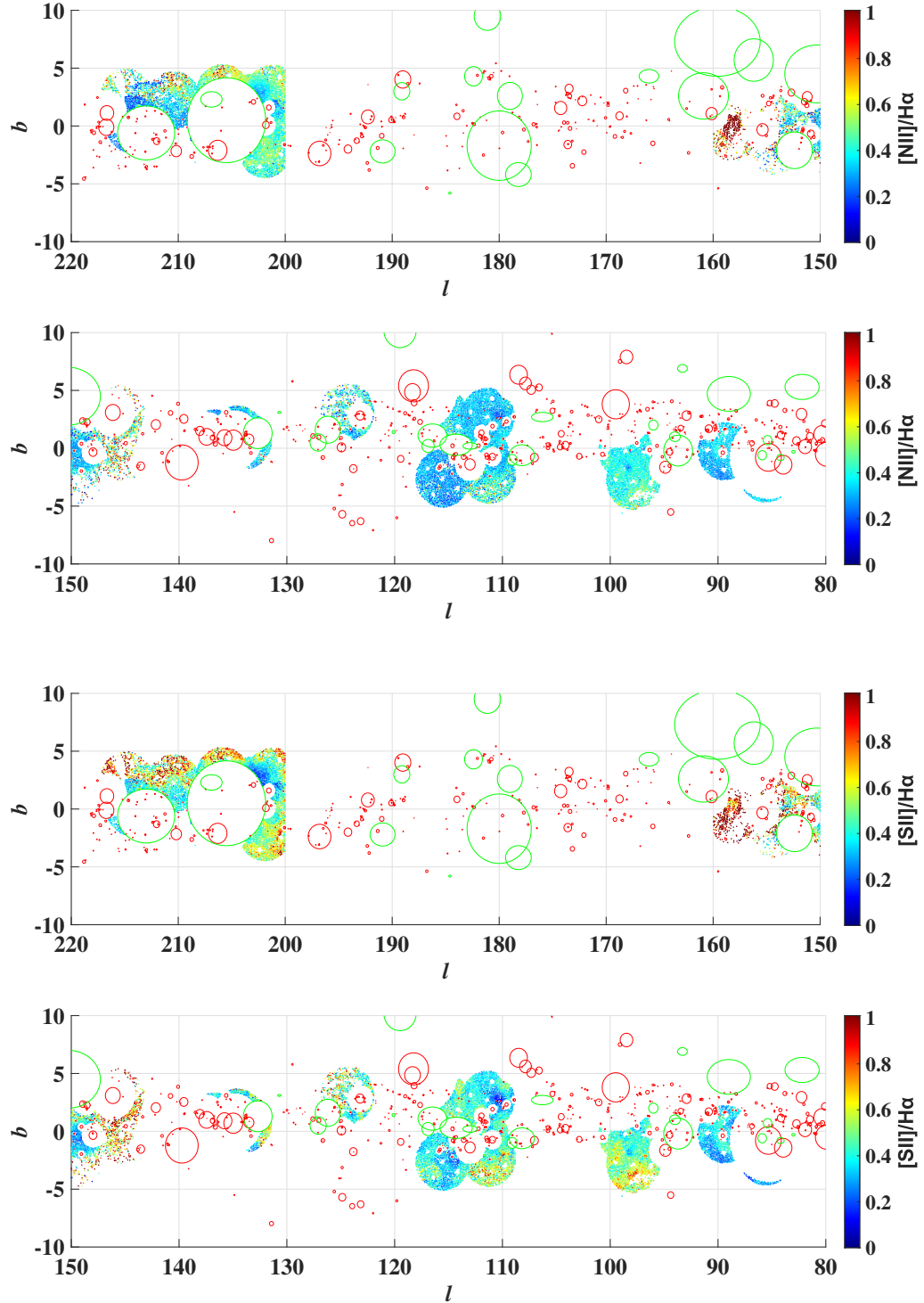


Figure 2. Spatial distribution of the Galactic DIG sample (Sample-I). Red circles represent the HII regions sourced from the WISE HII catalog by Anderson et al. (2014), while the green circles correspond to the SNRs listed in the catalog by Green (2019). Upper two panels: colored by $[N II]/H\alpha$ ratios; bottom two panels: colored by $[S II]/H\alpha$ ratios.

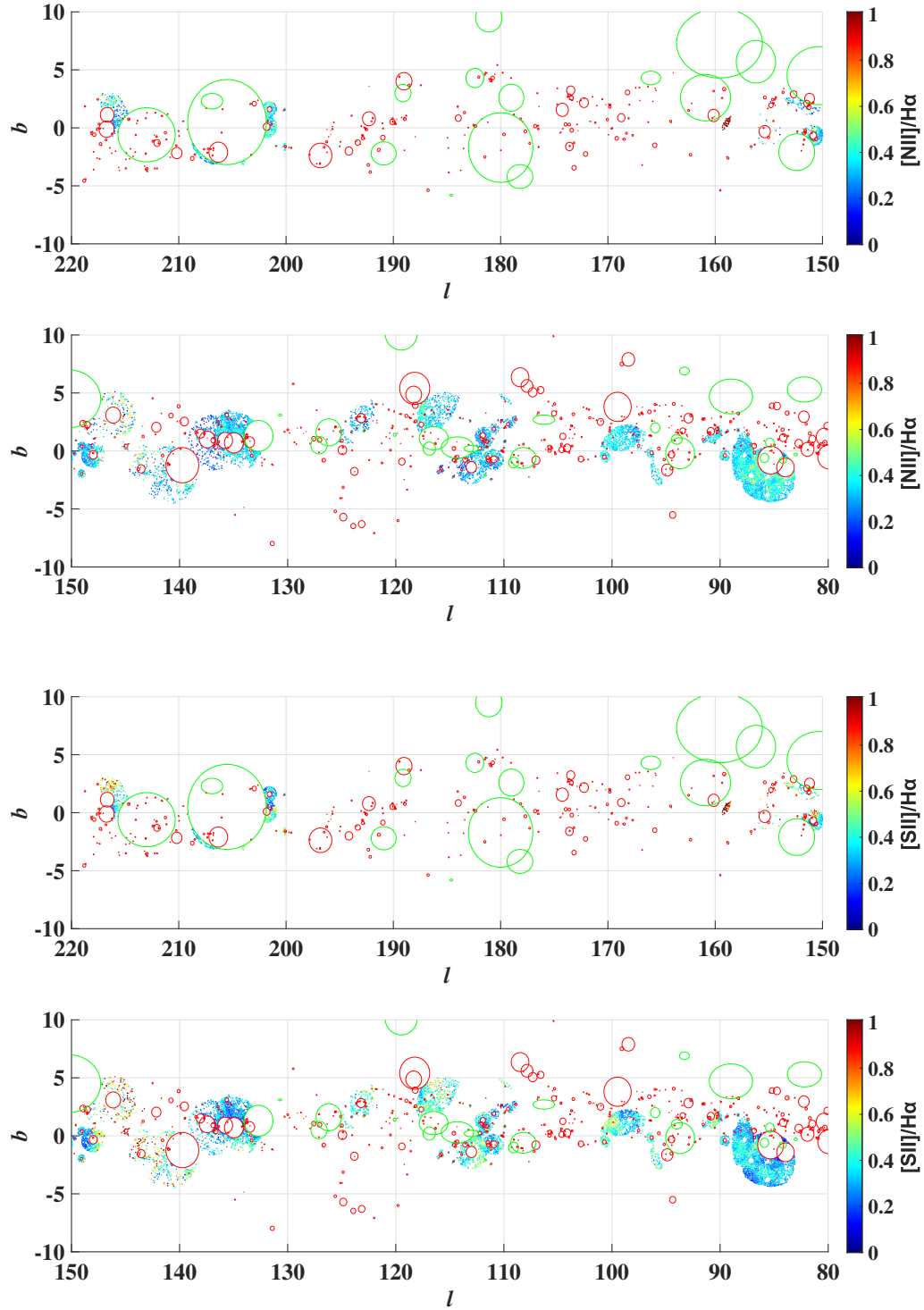


Figure 3. Same as Figure 2, but for the transition sample (Sample-II). Upper two panels: colored by $[N II]/H\alpha$ ratios; bottom two panels: colored by $[S II]/H\alpha$ ratios.

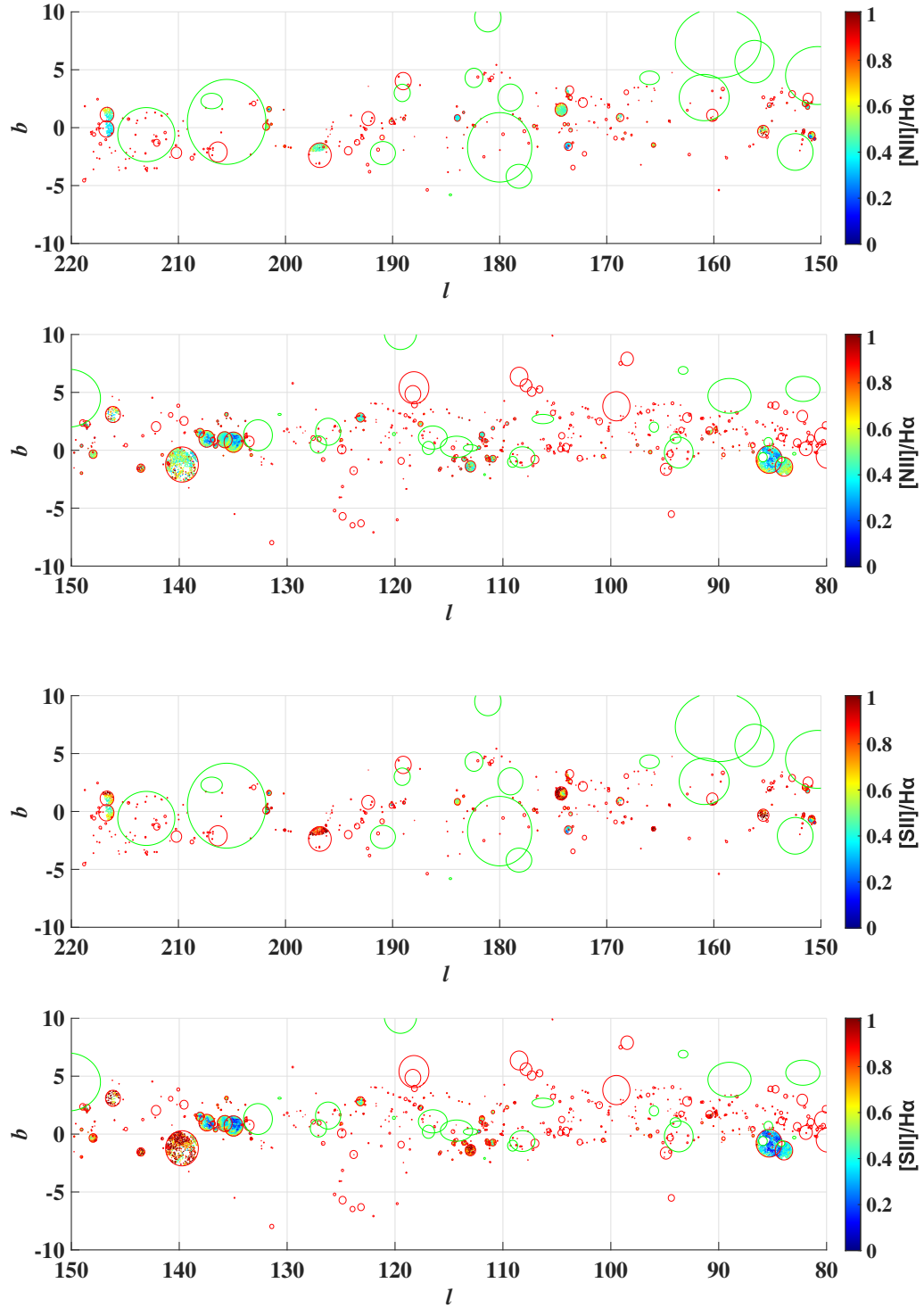


Figure 4. Same as Figure 2, but for HII regions. Upper two panels: colored by $[\text{N II}]/\text{H}\alpha$ ratios; bottom two panels: colored by $[\text{S II}]/\text{H}\alpha$ ratios.

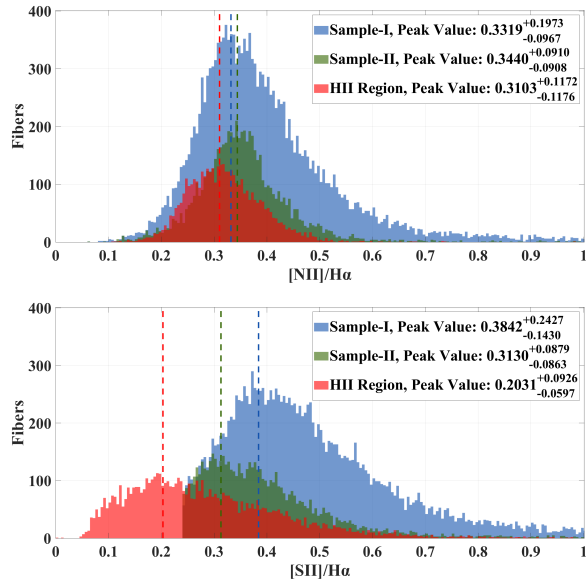


Figure 5. Histogram distribution of $[\text{N II}]/\text{H}\alpha$ and $[\text{S II}]/\text{H}\alpha$ line ratios. The panels represent Sample-I, Sample-II, and HII regions with blue, green and red bars, respectively. Dashed line indicates the distribution’s peak. The regions to the left and right of this peak are individually fitted with Gaussian profiles. The 1σ values of the Gaussians are annotated in the upper-right corner of each panel.

$[\text{S II}]/\text{H}\alpha$ line ratio. Red circles denote the region defined by the WISE HII catalog, while green circles represent the regions of SNRs as defined by Green (2019).

In order to compare the properties of DIG with the gas adjacent to HII regions and infer the effects of the HII regions, we construct another sample. This sample is selected using similar criteria, with the additional requirement that the fibers are located within 1-3 times the HII radii, and also remove fibers with $[\text{S II}]/\text{H}\alpha < 0.24$. This resulting sample consists of 6,925 fibers and is denoted as Sample-II. Sample-II can be considered as the transitional regions between HII regions and DIG regions. By applying criteria (1) and (2) and ensuring that at least one fiber is located within the WISE HII radius region, we constructed a large sample of ~ 300 HII regions as targets. We retained sources within the range of $160 \leq l \leq 200$, as we opted to utilize combined distance measures such as parallax distance of ionizing OB central stars, 3D extinction distance, velocity dispersion versus size relation, and kinematic distance when uncertainty is small enough. Since the S/N of the spectra for HII regions is relatively higher than that of DIG, and to retain more spectra for the HII regions, we resample the HII sample into $3' \times 3'$ bins. As a result, the HII regions consist of 5,420 individual fibers. Details of this sample will be presented in Zhao et al. (in preparation).

The spatial distribution of sample-II and HII regions are shown in Figure 3.

The histogram distributions of the line ratios of $[\text{N II}]/\text{H}\alpha$ and $[\text{S II}]/\text{H}\alpha$ of Sample-I are showed in Figure 5 as blue bars. To facilitate a comparison between DIG, HII regions and the transitional regions between them, the histogram distributions of these two line ratios of Sample-II and HII regions are presented in the same panels as green and red bars.

The analysis reveals that the DIG sample have exhibits a $[\text{N II}]/\text{H}\alpha$ flux ratio with a peak at 0.33, a little higher than that for HII regions which peaks at 0.31. For the $[\text{S II}]/\text{H}\alpha$ line ratio of DIG displays a peak at 0.38, is significantly higher than HII regions of 0.20. This result is consistent with the well-established finding that DIG exhibits enhanced $[\text{N II}]/\text{H}\alpha$ and $[\text{S II}]/\text{H}\alpha$ ratios compared to classical HII regions (e.g., Madsen et al. 2006), suggesting that DIG is warmer than HII regions (e.g., Haffner et al. 2009) and that the DIG spectrum is dominated by low ionization states (Zurita et al. 2000). Besides, compared to Sample-II and HII regions, Sample-I do not show a much wider distribution range of the line ratios of $[\text{S II}]/\text{H}\alpha$ and $[\text{N II}]/\text{H}\alpha$.

3. PARAMETER CALCULATION

3.1. Kinematic Distance

As the ionization source is not always specified – often being a combination of contributions from HII regions, HOLMES, SNRs, and others – it is challenging to identify the ionization source and use its distance as the distance to Galactic DIG. Simultaneously, DIG tends to be located in lower-density environments, making it impossible to derive the distance based on the 3D reddening map. Therefore, the only viable method, and perhaps the most plausible one, is the kinematic distance method. Although DIG in LAMOST MRS-N does not suffer from the kinematic distance ambiguity (KDA), the uncertainty of such distances can be as high as 50% for sources within 20 degrees of the Galactic anti-center (Anderson et al. 2014). This is why we have removed the sources in the range of $160^\circ \leq l \leq 200^\circ$ from our sample. The local standard of rest (LSR) velocity (VLSR) has been transferred from heliocentric velocity by adopting the motion of the Sun in the LSR, which is moving at a speed of about 20 km s^{-1} towards (RA = 18h03m50.29s, DEC = +30°00'16.8") at epoch 2000. The kinematic distances are derived using the Python package downloaded from <https://github.com/tvwenger/kd> (Wenger et al. 2018). During the calculation, the rotation curve by Reid et al. (2014) is adopted. The Galactocentric distance (R_{gal})

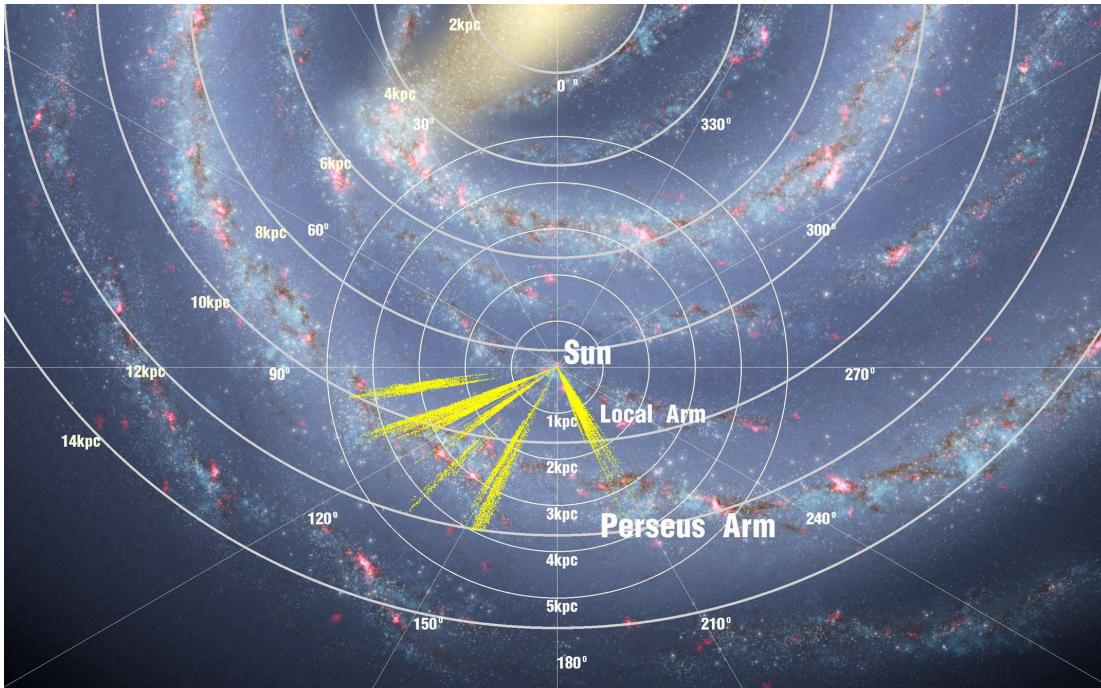


Figure 6. Plan view of the disk DIG from the north Galactic pole, display the projection of the sample points on the galactic disk. The Galactic center is taken as the origin point, and the direction from the Sun to the Galactic center is taken as the polar coordinate starting direction, and radial unit is kpc. We mark the location of Solar system at the Galactocentric distance of 8.34 kpc. Background image credit: NASA/JPL-Caltech/ESO/R. Hurt

is calculated by adopting $R_{\odot} = 8.34$ kpc. The plan view of the Sample-I is shown in Figure 6.

3.2. Oxygen Abundance

The wavelength range covered by the LAMOST MRS-N data enables us to use three indirect metallicity calibrators, N2 (Pettini & Pagel 2004), S2 (Curti et al. 2020) and N2S2H α (Dopita et al. 2016). However, N2 method is not applicable in the DIG region, as the N2–metallicity calibration saturates and flattens at the BPT boundary between H II regions and low ionized regions (LIERs) (Curti et al. 2020; Kumari et al. 2019). In this work, we prefer to use [N II]/H α and [S II]/H α line ratios to investigate their variations across the Galactic disk rather than employing them to estimate the metallicity. Given N2S2H α method is insensitivity to changes in the ionization parameter, owing to the inclusion of the [N II]/[S II] emission line ratio (Poetrodjojo et al. 2019), we employ the N2S2H α method to estimate the oxygen abundance as follows:

$$12 + \log(\text{O}/\text{H}) = 8.77 + \log([\text{N II}]/[\text{S II}]) + 0.264 \times \log([\text{N II}]/\text{H}\alpha) \quad (1)$$

4. RADIAL AND VERTICAL DISTRIBUTIONS OF LINE RATIOS, AND OXYGEN ABUNDANCE

4.1. Radial distribution

We explore the line ratios of [N II]/H α , [S II]/H α , and [S II]/[N II] as functions of R_{gal} in panels of the first and second rows in Figure 7. The linear fitting results are summarized in Table 1.

For clarity in illustrating the trend, we divided the data into bins based on R_{gal} , and display the median value along with 1σ dispersion of each bin. Interestingly, neither [N II]/H α nor [S II]/H α demonstrates a consistent, monotonous decrease with increasing R_{gal} . Instead, they peaks at ~ 9.1 kpc, within the interarm region between the Local arm and the Perseus arm. This peculiarity may be attributed to differences in the ionization mechanisms between interarm regions and the arms, potentially due to a substantial presence of HOLMES in the interarm region. Because of the non-monotonic trends, therefore, rather than attempting a least squares fitting of the data to derive possible slopes, we opt to simply connect the median values using a dashed line.

The line ratio of [S II]/[N II] is presented alongside R_{gal} in the panel of the third row in Figure 7. It's found that [S II]/[N II] increase with R_{gal} , exhibiting a a steep incline in the inner disk, and maintaining nearly constancy in the outer disk. The disk is then divided into inner and outer regions, using a cut-off at $R_{gal} = 9.65$

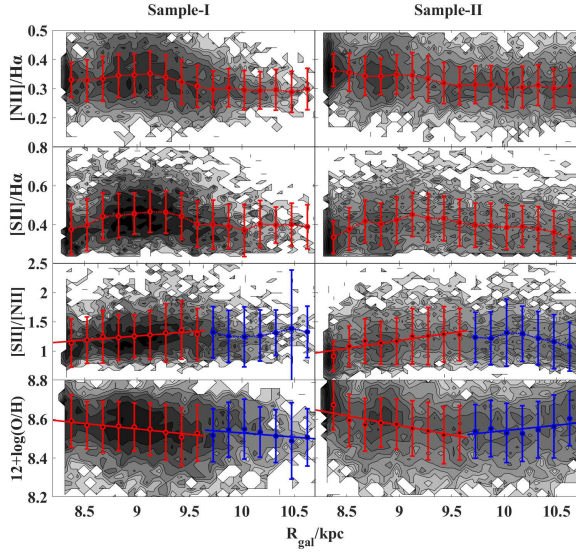


Figure 7. Radial distributions of $[\text{N II}]/\text{H}\alpha$, $[\text{S II}]/\text{H}\alpha$, $[\text{S II}]/[\text{N II}]$ line ratios, and oxygen abundance as a function of R_{gal} . The data are organized into 16 bins based on R_{gal} , and a dashed line connects the median value of each bin. The results of Sample-I and Sample-II are illustrated in the left and right panels, respectively.

kpc. Linear fittings of the trend in the inner disk yield with a slope of $0.1415 \pm 0.0646 \text{ kpc}^{-1}$.

We examine the radial distributions of oxygen abundance in bottom two panels in Figure 7. The oxygen abundance demonstrates an inverse trend with R_{gal} in the inner disk, with a slope of $-0.0559 \pm 0.0209 \text{ dex kpc}^{-1}$, while exhibiting a comparable pattern in the outer region, characterized by a slope of $-0.0429 \pm 0.0599 \text{ dex kpc}^{-1}$. A single linear fitting to the entire disk yields a slope of $-0.0317 \pm 0.0124 \text{ dex kpc}^{-1}$.

To explore the potential distribution differences between Sample-I and Sample-II, we show the radial distribution of Sample-II in the right panels of Figure 7. It is found that $[\text{N II}]/\text{H}\alpha$ gradually decreases with increasing R_{gal} . For the remaining distributions, Sample-II exhibits similar trends to Sample-I. However, the slopes in the inner region are slightly steeper than that of Sample-I.

4.2. Vertical distribution

Based on WHAM data, Haffner et al. (1999) have investigated the vertical distribution of DIG. They found that the intensity of $\text{H}\alpha$ emission decreases as distance from the Galactic midplane increases. Additionally, the line ratios of $[\text{N II}]/\text{H}\alpha$ and $[\text{S II}]/\text{H}\alpha$ increase with increasing $|z|$.

In Figure 8, we examine the vertical distributions of line ratios and oxygen abundance of Sample-I and

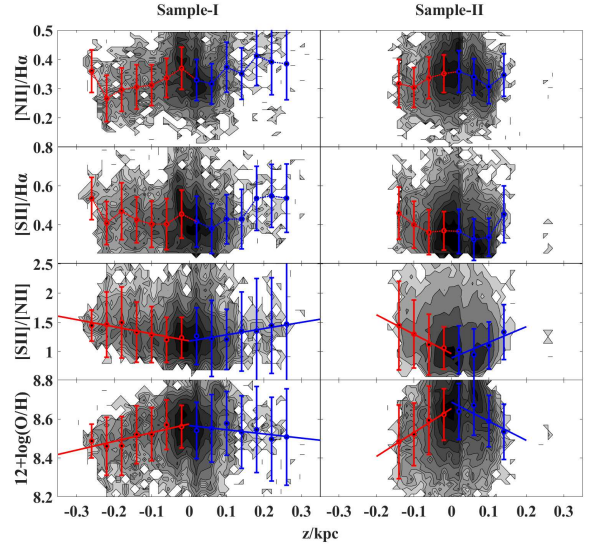


Figure 8. Similar to Figure 7, with the variation plotted as a function of Galactic disk height (z).

Sample-II. As these samples are located within a distance of less than 2.5 kpc from us, and the survey is constrained to $|b| \leq 5^\circ$, they are predominantly situated in the thin disk. Sample-II, selected from regions adjacent to HII regions, is further restricted to even smaller heights from the midplane, with $|z| < 0.15 \text{ kpc}$, compared to $|z| < 0.3 \text{ kpc}$ for Sample-I.

In the left panels in Figure 8, we examine the vertical distributions of line ratios and oxygen abundance of Sample-I. We confirmed that the $[\text{N II}]/\text{H}\alpha$ and $[\text{S II}]/\text{H}\alpha$ line ratios increase with increasing $|z|$. In comparison, the $[\text{S II}]/[\text{N II}]$ ratio shows a more pronounced trend along the vertical direction, with slopes of $1.2093 \pm 0.7067 \text{ kpc}^{-1}$ and $1.0688 \pm 0.6047 \text{ kpc}^{-1}$ in the southern and northern disks, respectively. Additionally, oxygen abundance is highest at the midplane and decreases with increasing $|z|$, with slopes of $-0.4476 \pm 0.2833 \text{ dex kpc}^{-1}$ and $-0.2150 \pm 0.2640 \text{ dex kpc}^{-1}$ in the southern and northern disks, respectively.

For comparison, Figure 8 presents the results of Sample-II in its right panels. Compared to Sample-I, Sample-II shows comparable slopes for both the $[\text{S II}]/[\text{N II}]$ ratio and oxygen abundance: $3.3214 \pm 1.9115 \text{ dex kpc}^{-1}$ and $2.6809 \pm 5.5085 \text{ dex kpc}^{-1}$ for $[\text{S II}]/[\text{N II}]$ ratio in the southern and northern disks, respectively, and $-1.2302 \pm 0.5969 \text{ dex kpc}^{-1}$ and $-0.9834 \pm 1.8094 \text{ dex kpc}^{-1}$ for oxygen abundance in these regions.

Detailed results of the linear fits are summarized in Table 2. The differences in slopes between the southern and northern disks can be attributed to two main factors: 1) incomplete coverage of the current sample

across the disk, and 2) the separation of the southern and northern disk is dependent on R_{gal} owing to the wrap structure of the Galactic disk. In our upcoming work, we plan to further analyze these trends using a larger dataset that provides continuous coverage.

5. DISCUSSION

5.1. Oxygen Abundance

Radial abundance gradients in the Galactic disk have been extensively investigated using various tracers, including open clusters, HII regions, PNe, and other stellar objects. In this work, the LAMOST MRS-N provides DIG as a new tracer to facilitate similar analyses and to compare the results with those obtained using HII regions.

In optical bands, oxygen abundances are accurately determined using the direct T_e -method, whereas the strong emission line method exhibits comparatively larger scatter. Conversely, in radio bands, T_e can be measured with high precision ($\sim 1\%$) using RRL and radio continuum, enabling the derivation of oxygen abundances through the tight oxygen- T_e relationship.

Earlier studies by [Balsler et al. \(2011\)](#) determined an oxygen abundance gradient of -0.0446 ± 0.0049 dex kpc^{-1} for 133 HII regions observed at National Radio Astronomy Observatory (NRAO). Among later works, [Wenger et al. \(2019\)](#) observed radio emissions from 82 HII regions observed by the Very Large Array (VLA) at NRAO, derived an oxygen abundance gradient of -0.052 ± 0.004 dex kpc^{-1} . [Arellano-Córdova et al. \(2021\)](#) obtained an oxygen abundance gradient of 0.042 ± 0.009 dex kpc^{-1} based on combined sample of 42 Galactic HII regions observed by the Gran Telescopio Canarias telescope and collected from public data. [Méndez-Delgado et al. \(2022\)](#) recalibrated the distances to these 42 HII regions using Gaia EDR3 data, and derive the radial gradient for oxygen as -0.044 ± 0.009 dex kpc^{-1} . [Wang et al. \(2018\)](#) fitted the metallicity gradient of the HII regions of the whole Galactic disk and the outer disk ($R_{gal} \geq 11.5kpc$), calculated radial gradients of -0.036 ± 0.004 dex kpc^{-1} .

We adopt the N2S2H α method discussed in [Dopita et al. \(2016\)](#) to measure oxygen abundance for both Sample-I and Sample-II. In Sample-I, there is no evidence of a flattened gradient in the outer disk. Employing a single slope fitting yields an oxygen abundance radial gradient with a slope of -0.0317 ± 0.0124 dex kpc^{-1} , comparable to that observed in HII regions. In Sample-II, a clear two-slope pattern emerges, with the inner disk exhibiting a steeper slope than that of HII regions, while the outer disk shows nearly flat behavior.

It should be noted that the N2S2H α method is calibrated based on assumptions about photoionization models. However, DIG encompasses various energy sources and cannot be accurately modeled solely by photoionization models. Therefore, applying the N2S2H α method to DIG may introduce unknown biases that need to be assessed using specific models designed for DIG in future studies.

5.2. Variation of [S II]/[N II] ratio

The ratio [N II]/H α in DIG regions is enhanced compared to that in HII regions, which can be attributed to the sensitivity of [N II]/H α to T_e ([Haffner et al. 2009](#)). According to the ionization potential of N (14.5 eV) and N $^+$ (29.6 eV), it is implied that most of N in the DIG region is likely to be in the form of N $^+$ and only a small fraction of nitrogen exists as N $^{++}$ ([Madsen et al. 2006](#)). On the other hand, the ionization potential of S $^+$ is stated to be 23.4 eV, suggesting that a significant fraction of S may be present in the form of S $^{++}$. The quantity [S II]/H α is described as a combination of T_e and S $^+$ /S. The trend of [S II]/[N II] versus H α intensity is reported to be relatively flat, implying that it is less sensitive to changes in T_e ([Haffner et al. 1999](#)). Hereafter, the trend of [S II]/[N II] along the Galactic plane shown in [Figure 7](#) should not be caused by the increasing T_e with R_{gal} . Instead, it indicates that the ratio of S $^+$ /S undergoes a systematic change with R_{gal} . That is, in the outer disk, a higher fraction of sulfur exists in the form of S $^{++}$.

6. SUMMARY

We constructed a large DIG sample towards the anti-galactic center based on LAMOST MRS-N data and investigate the radial and vertical distribution of the line ratios, including [N II]/H α , [S II]/H α , [S II]/[N II], and oxygen abundance. Our main results are summarized as follows:

- (1) The line ratios of [N II]/H α and [S II]/H α initially increase with R_{gal} and then decrease, exhibiting a turnover point at approximately 9.1 kpc. This position corresponds to the interarm region, situated between the Local Arm and the Perseus Arm. This suggests a distinct ionizing mechanism between the DIG in the spiral arm and the interarm region.
- (2) The [S II]/[N II] ratio initially rises with R_{gal} in inner disk ($8.34 kpc < R_{gal} < 9.65 kpc$) with a slope of $0.1415 \pm 0.0646 kpc^{-1}$, and then flatten out in the outer region, implying a higher ratio of S $^+$ /S in the outer disk.

- (3) The oxygen abundance is estimated using the N2S2H α method, which combines [S II]/[N II] and [N II]/H α ratios. The resulting oxygen abundance exhibits a comparable trend in both the inner and outer disk regions, showing slopes of -0.0559 ± 0.0209 dex kpc $^{-1}$ and -0.0429 ± 0.0599 dex kpc $^{-1}$, respectively. This trend can be described by a singular linear fit with a slope of -0.0317 ± 0.0124 dex kpc $^{-1}$.
- (4) Despite the current sample being confined to the thin disk with $|z| < 0.3$ kpc, we confirm that both [N II]/H α and [S II]/H α line ratios increase with increasing $|z|$ in both northern and southern disk. Additionally, [S II]/[N II] shows a more distinct trend, while the oxygen abundance exhibits an opposite trend.

We possess a substantial sample of Galactic DIG. However, a notable limitation is the presence of substantial gaps between the observational plates, and these plates are not uniformly distributed across the Galactic disk. The asymmetrical distribution of DIG parameters found in our study between the southern and northern disks is likely due to constraints imposed by the cur-

rent dataset and the the warp structure of the Galactic disk. To tackle these challenges, our plan is to improve our analysis by integrating additional survey data in our upcoming work.

ACKNOWLEDGMENTS

This work is supported by the National Natural Science Foundation of China (NSFC) (No. 12090041; 12090040) and the National Key R&D Program of China grant (No. 2021YFA1600401; 2021YFA1600400). This work is also sponsored by the Strategic Priority Research Program of the Chinese Academy of Sciences (No. XDB0550100). Guoshoujing Telescope (the Large Sky Area Multi-Object Fiber Spectroscopic Telescope LAMOST) is a National Major Scientific Project built by the Chinese Academy of Sciences. Funding for the project has been provided by the National Development and Reform Commission. LAMOST is operated and managed by the National Astronomical Observatories, Chinese Academy of Sciences.

REFERENCES

- Anderson, L. D., Bania, T. M., Balsaer, D. S., et al. 2014, *ApJS*, 212, 1, doi: [10.1088/0067-0049/212/1/1](https://doi.org/10.1088/0067-0049/212/1/1)
- Anderson, L. D., Luisi, M., Liu, B., et al. 2021, *ApJS*, 254, 28, doi: [10.3847/1538-4365/abef65](https://doi.org/10.3847/1538-4365/abef65)
- Arellano-Córdova, K. Z., Esteban, C., García-Rojas, J., & Méndez-Delgado, J. E. 2021, *MNRAS*, 502, 225, doi: [10.1093/mnras/staa3903](https://doi.org/10.1093/mnras/staa3903)
- Baldwin, J. A., Phillips, M. M., & Terlevich, R. 1981, *PASP*, 93, 5, doi: [10.1086/130766](https://doi.org/10.1086/130766)
- Balsaer, D. S., Rood, R. T., Bania, T. M., & Anderson, L. D. 2011, *ApJ*, 738, 27, doi: [10.1088/0004-637X/738/1/27](https://doi.org/10.1088/0004-637X/738/1/27)
- Belfiore, F., Maiolino, R., Maraston, C., et al. 2016, *MNRAS*, 461, 3111, doi: [10.1093/mnras/stw1234](https://doi.org/10.1093/mnras/stw1234)
- Belfiore, F., Santoro, F., Groves, B., et al. 2022, *A&A*, 659, A26, doi: [10.1051/0004-6361/202141859](https://doi.org/10.1051/0004-6361/202141859)
- Collins, J. A., & Rand, R. J. 2001, *ApJ*, 551, 57, doi: [10.1086/320072](https://doi.org/10.1086/320072)
- Cui, X.-Q., Zhao, Y.-H., Chu, Y.-Q., et al. 2012, *Research in Astronomy and Astrophysics*, 12, 1197, doi: [10.1088/1674-4527/12/9/003](https://doi.org/10.1088/1674-4527/12/9/003)
- Curti, M., Mannucci, F., Cresci, G., & Maiolino, R. 2020, *MNRAS*, 491, 944, doi: [10.1093/mnras/stz2910](https://doi.org/10.1093/mnras/stz2910)
- Della Bruna, L., Adamo, A., Amram, P., et al. 2022, *A&A*, 660, A77, doi: [10.1051/0004-6361/202142315](https://doi.org/10.1051/0004-6361/202142315)
- Dopita, M. A., Kewley, L. J., Sutherland, R. S., & Nicholls, D. C. 2016, *Astrophysics and Space Science*, 361, doi: [10.1007/s10509-016-2657-8](https://doi.org/10.1007/s10509-016-2657-8)
- Draine, B. T. 2011, *Physics of the Interstellar and Intergalactic Medium*
- Esteban, C., Fang, X., García-Rojas, J., & Toribio San Cipriano, L. 2017, *MNRAS*, 471, 987, doi: [10.1093/mnras/stx1624](https://doi.org/10.1093/mnras/stx1624)
- Flores-Fajardo, N., Morisset, C., Stasińska, G., & Binette, L. 2011, *MNRAS*, 415, 2182, doi: [10.1111/j.1365-2966.2011.18848.x](https://doi.org/10.1111/j.1365-2966.2011.18848.x)
- Gerin, M., Ruaud, M., Goicoechea, J. R., et al. 2015, *A&A*, 573, A30, doi: [10.1051/0004-6361/201424349](https://doi.org/10.1051/0004-6361/201424349)
- Green, D. A. 2019, *Journal of Astrophysics and Astronomy*, 40, 36, doi: [10.1007/s12036-019-9601-6](https://doi.org/10.1007/s12036-019-9601-6)
- Haffner, L. M., Reynolds, R. J., & Tufte, S. L. 1999, *ApJ*, 523, 223, doi: [10.1086/307734](https://doi.org/10.1086/307734)
- Haffner, L. M., Reynolds, R. J., Tufte, S. L., et al. 2003, *ApJS*, 149, 405, doi: [10.1086/378850](https://doi.org/10.1086/378850)
- Haffner, L. M., Dettmar, R. J., Beckman, J. E., et al. 2009, *Reviews of Modern Physics*, 81, 969, doi: [10.1103/RevModPhys.81.969](https://doi.org/10.1103/RevModPhys.81.969)
- Hausen, N. R., Reynolds, R. J., & Haffner, L. M. 2002, *AJ*, 124, 3336, doi: [10.1086/344603](https://doi.org/10.1086/344603)

- Hou, L., Han, J., Hong, T., Gao, X., & Wang, C. 2022, *Science China Physics, Mechanics, and Astronomy*, 65, 129703, doi: [10.1007/s11433-022-2039-8](https://doi.org/10.1007/s11433-022-2039-8)
- Hoyle, F., & Ellis, G. R. A. 1963, *Australian Journal of Physics*, 16, 1, doi: [10.1071/PH630001](https://doi.org/10.1071/PH630001)
- Kaplan, K. F., Jogee, S., Kewley, L., et al. 2016, *MNRAS*, 462, 1642, doi: [10.1093/mnras/stw1422](https://doi.org/10.1093/mnras/stw1422)
- Kauffmann, G., Heckman, T. M., Tremonti, C., et al. 2003, *MNRAS*, 346, 1055, doi: [10.1111/j.1365-2966.2003.07154.x](https://doi.org/10.1111/j.1365-2966.2003.07154.x)
- Kewley, L. J., Groves, B., Kauffmann, G., & Heckman, T. 2006, *MNRAS*, 372, 961, doi: [10.1111/j.1365-2966.2006.10859.x](https://doi.org/10.1111/j.1365-2966.2006.10859.x)
- Kulkarni, S. R., Beichman, C., & Ressler, M. E. 2024, *PASP*, 136, 054301, doi: [10.1088/1538-3873/ace6d9](https://doi.org/10.1088/1538-3873/ace6d9)
- Kumari, N., Maiolino, R., Belfiore, F., & Curti, M. 2019, *MNRAS*, 485, 367, doi: [10.1093/mnras/stz366](https://doi.org/10.1093/mnras/stz366)
- Langer, W. D., Velusamy, T., Goldsmith, P. F., et al. 2017, *A&A*, 607, A59, doi: [10.1051/0004-6361/201731198](https://doi.org/10.1051/0004-6361/201731198)
- Liu, C., Fu, J., Shi, J., et al. 2020, arXiv e-prints, arXiv:2005.07210, doi: [10.48550/arXiv.2005.07210](https://doi.org/10.48550/arXiv.2005.07210)
- Luisi, M., Anderson, L. D., Balser, D. S., Wenger, T. V., & Bania, T. M. 2017, *ApJ*, 849, 117, doi: [10.3847/1538-4357/aa8fd2](https://doi.org/10.3847/1538-4357/aa8fd2)
- Luisi, M., Anderson, L. D., Liu, B., Anish Roshi, D., & Churchwell, E. 2019, *ApJS*, 241, 2, doi: [10.3847/1538-4365/aaf6a5](https://doi.org/10.3847/1538-4365/aaf6a5)
- Luo, A. L., Zhao, Y.-H., Zhao, G., et al. 2015, *Research in Astronomy and Astrophysics*, 15, 1095, doi: [10.1088/1674-4527/15/8/002](https://doi.org/10.1088/1674-4527/15/8/002)
- Madsen, G. J., Reynolds, R. J., & Haffner, L. M. 2006, *ApJ*, 652, 401, doi: [10.1086/508441](https://doi.org/10.1086/508441)
- Méndez-Delgado, J. E., Amayo, A., Arellano-Córdova, K. Z., et al. 2022, *MNRAS*, 510, 4436, doi: [10.1093/mnras/stab3782](https://doi.org/10.1093/mnras/stab3782)
- Persson, C. M., Gerin, M., Mookerjee, B., et al. 2014, *A&A*, 568, A37, doi: [10.1051/0004-6361/201423997](https://doi.org/10.1051/0004-6361/201423997)
- Pettini, M., & Pagel, B. E. J. 2004, *MNRAS*, 348, L59, doi: [10.1111/j.1365-2966.2004.07591.x](https://doi.org/10.1111/j.1365-2966.2004.07591.x)
- Poetrodjojo, H., D'Agostino, J. J., Groves, B., et al. 2019, *MNRAS*, 487, 79, doi: [10.1093/mnras/stz1241](https://doi.org/10.1093/mnras/stz1241)
- Reid, M. J., Menten, K. M., Brunthaler, A., et al. 2014, *ApJ*, 783, 130, doi: [10.1088/0004-637X/783/2/130](https://doi.org/10.1088/0004-637X/783/2/130)
- Ren, J.-J., Wu, H., Wu, C.-J., et al. 2021, *Research in Astronomy and Astrophysics*, 21, 051, doi: [10.1088/1674-4527/21/3/51](https://doi.org/10.1088/1674-4527/21/3/51)
- Reynolds, R. J. 1991, in *The Interstellar Disk-Halo Connection in Galaxies*, ed. H. Bloemen, Vol. 144, 67
- Reynolds, R. J., Haffner, L. M., & Tuftte, S. L. 1999, *ApJ*, 525, L21, doi: [10.1086/312326](https://doi.org/10.1086/312326)
- Reynolds, R. J., Hausen, N. R., Tuftte, S. L., & Haffner, L. M. 1998, *ApJ*, 494, L99, doi: [10.1086/311154](https://doi.org/10.1086/311154)
- Reynolds, R. J., Scherb, F., & Roesler, F. L. 1973, *ApJ*, 185, 869, doi: [10.1086/152461](https://doi.org/10.1086/152461)
- Sanders, R. L., Shapley, A. E., Zhang, K., & Yan, R. 2017, *ApJ*, 850, 136, doi: [10.3847/1538-4357/aa93e4](https://doi.org/10.3847/1538-4357/aa93e4)
- Sparke, L. S., & Gallagher, John S., I. 2007, *Galaxies in the Universe*
- Su, D.-Q., & Cui, X.-Q. 2004, *ChJAA*, 4, 1, doi: [10.1088/1009-9271/4/1/1](https://doi.org/10.1088/1009-9271/4/1/1)
- Velusamy, T., Langer, W. D., Goldsmith, P. F., & Pineda, J. L. 2015, *A&A*, 578, A135, doi: [10.1051/0004-6361/201525902](https://doi.org/10.1051/0004-6361/201525902)
- Velusamy, T., Langer, W. D., Pineda, J. L., & Goldsmith, P. F. 2012, *A&A*, 541, L10, doi: [10.1051/0004-6361/201219303](https://doi.org/10.1051/0004-6361/201219303)
- Wang, L.-L., Luo, A. L., Hou, W., et al. 2018, *PASP*, 130, 114301, doi: [10.1088/1538-3873/aadf22](https://doi.org/10.1088/1538-3873/aadf22)
- Wang, S.-G., Su, D.-Q., Chu, Y.-Q., Cui, X., & Wang, Y.-N. 1996, *ApOpt*, 35, 5155, doi: [10.1364/AO.35.005155](https://doi.org/10.1364/AO.35.005155)
- Wenger, T. V., Balser, D. S., Anderson, L. D., & Bania, T. M. 2018, *ApJ*, 856, 52, doi: [10.3847/1538-4357/aaaec8](https://doi.org/10.3847/1538-4357/aaaec8)
- . 2019, *ApJ*, 887, 114, doi: [10.3847/1538-4357/ab53d3](https://doi.org/10.3847/1538-4357/ab53d3)
- Wright, E. L., Eisenhardt, P. R. M., Mainzer, A. K., et al. 2010, *AJ*, 140, 1868, doi: [10.1088/0004-6256/140/6/1868](https://doi.org/10.1088/0004-6256/140/6/1868)
- Wu, C.-J., Wu, H., Zhang, W., et al. 2021, *Research in Astronomy and Astrophysics*, 21, 096, doi: [10.1088/1674-4527/21/4/96](https://doi.org/10.1088/1674-4527/21/4/96)
- . 2022, *Research in Astronomy and Astrophysics*, 22, 075015, doi: [10.1088/1674-4527/ac7387](https://doi.org/10.1088/1674-4527/ac7387)
- Yan, R., & Blanton, M. R. 2012, *ApJ*, 747, 61, doi: [10.1088/0004-637X/747/1/61](https://doi.org/10.1088/0004-637X/747/1/61)
- Zhang, K., Yan, R., Bundy, K., et al. 2017, *MNRAS*, 466, 3217, doi: [10.1093/mnras/stw3308](https://doi.org/10.1093/mnras/stw3308)
- Zhang, W., Wu, H., Wu, C.-J., et al. 2021, *Research in Astronomy and Astrophysics*, 21, 280, doi: [10.1088/1674-4527/21/11/280](https://doi.org/10.1088/1674-4527/21/11/280)
- Zhao, G., Zhao, Y.-H., Chu, Y.-Q., Jing, Y.-P., & Deng, L.-C. 2012, *Research in Astronomy and Astrophysics*, 12, 723, doi: [10.1088/1674-4527/12/7/002](https://doi.org/10.1088/1674-4527/12/7/002)
- Zurita, A., Rozas, M., & Beckman, J. E. 2000, *A&A*, 363, 9

Table 1. Radial fitting results of each sample.

Samples	Parameters	Radial Gradient			
		a(inner)(kpc ⁻¹)	b(inner)	a(outer)(kpc ⁻¹)	b(outer)
Sample-I	[S II]/[N II]	0.1415±0.0646	-0.0169±0.5806		
	12+log(O/H)(dex)	-0.0559±0.0209	9.0528±0.1881	-0.0429±0.0599	8.9578±0.6093
Sample-II	[S II]/[N II]	0.2662±0.1147	-1.2174±1.0307		
	12+log(O/H)(dex)	-0.0994±0.0462	9.4631±0.4148	0.0559±0.0677	7.9815±0.6887

Notes: The linear fitting function takes the form $y = a \times R_{gal} + b$. The inner disk is defined for $8.34 < R_{gal} < 9.65$ kpc, while the outer disk is indicated by $R_{gal} > 9.65$ kpc.

Table 2. Vertical fitting results of each sample.

Samples	Parameters	Vertical Gradient			
		a(south)(kpc ⁻¹)	b(south)	a(north)(kpc ⁻¹)	b(north)
Sample-I	[S II]/[N II]	1.2093±0.7067	1.1823±0.1139	1.0688±0.6047	1.1790±0.0975
	12+log(O/H)(dex)	-0.4476±0.2833	8.5750±0.0457	-0.2150±0.2640	8.5667±0.0426
Sample-II	[S II]/[N II]	3.3214±1.9115	0.9644±0.1752	2.6809±5.5085	0.8884±0.5049
	12+log(O/H)(dex)	-1.2302±0.5969	8.6543±0.0547	-0.9834±1.8094	8.6872±0.1658

Notes: The linear fitting function takes the form $y = a \times |z| + b$. The northern and southern disks correspond to $z > 0$ and $z < 0$, respectively.